AIAA JOURNAL
Vol. 50, No. 8, August 2012

Simulation-Guided, Model-Based Feedback Flow Control for a Pitching Turret

R. D. Wallace,* P. R. Shea,* and M. N. Glauser†
Syracuse University, Syracuse, New York 13244-1240
and
V. Thirunavukkarasu‡ and H. A. Carlson§
Clear Science Corporation, Harford, New York 13784-0233

DOI: 10.2514/1.J051063

Closed-loop systems have been developed for controlling the flow above a three-dimensional turret while the hemispherical top of the turret rotates about the pitch axis. Separation and concomitant turbulence levels incurred through the pitching cycle were altered by suction jet slots circumscribing the aperture, which served as control input; an array of pressure sensors on the turret surface provided the controller with information about the state of the flow above the surface. The control objective was to minimize the separation and turbulence in the dynamic environment created by the articulating turret. The closed-loop control systems included dynamical and measurement-based estimators, regulators, filters, and compensators. These components were developed using both computational and experimental data, and the control systems were evaluated through a series of control-in-the-loop computation-fluid-dynamics simulations and wind-tunnel runs. The implementation of this suction flow-control system resulted in a decrease of fluctuating velocity over the flat optical aperture. Initial simple proportional and the advanced proportional-integral closed-loop control systems were able to decrease the fluctuating velocity more efficiently than the steady suction of open-loop control. The more-advanced closed-loop controllers showed a better ability to track the trends of the separation and turbulence levels as the hemisphere of the turret pitched. The development of the controller design and numerical demonstration of the closed-loop feedback system is described in a companion paper.

Nomenclature

A_1	=	time-invariant matrix coefficient associated with the estimation
$a_n(t)$	=	nth proper orthogonal decomposition mode temporal expansion coefficient
a_0	=	time-invariant coefficient constant
b_0, b_2	=	time-invariant coefficients associated with the control input
b_3, b_4	=	time-invariant coefficients associated with the rotation
DC	=	duty cycle
h	=	height of turret
J	=	cost function
$k_{1,2}$	=	control gains
N_{PIV}	=	number of particle image velocimetry snapshots
r	=	penalty weight
T	=	period
t	=	time
u	=	duty cycle percentage
$\dot{u}$	=	control input/duty cycle rate
u_{rms}	=	root mean square of the velocity
$u_{1,2}$	=	instantaneous velocity
$\bar{u}_{1,2}$	=	mean velocity
$\dot{\hat{\mathbf{x}}}$	=	dynamic estimator signal
$\hat{x}_n$	=	measurement estimator signal
$\mathbf{z}$	=	augmented state estimate
δ	=	boundary-layer thickness
$\dot{\eta}$	=	angular speed
$\ddot{\eta}$	=	angular acceleration
θ	=	pitch angle
ξ	=	controller efficiency
τ	=	time lag
ω	=	angular frequency

Presented at the 39th AIAA Fluid Dynamics Conference, Orlando, FL, 4–7 January 2010; received 24 February 2011; revision received 12 August 2011; accepted for publication 17 August 2011.

*Graduate Student, Department of Mechanical and Aerospace Engineering. Student Member AIAA.
†Professor, Department of Mechanical and Aerospace Engineering. Fellow AIAA.
‡Research Scientist, 663 Owego Hill Road.
§President, 663 Owego Hill Road.

I. Introduction

TURBULENCE, random density fluctuations, and aero-optical distortion in the flow around a turret can degrade the performance of a laser system housed within the turret. Laser light passing through the turbulent region is refracted by variations in density and optical path differences, scattering the light and reducing the laser intensity. One solution to the problem is to adapt the optical system in a way that compensates for the flow distortion, without altering the flow itself; for example, a morphing lens that keeps the laser focused in the presence of aero-optic distortions through contortions of the deformable mirror [1]. Another solution is to control (minimize), either actively or passively, the flow fluctuations that cause aero-optical distortion.

In a passive-flow control experiment, vortex generators mounted on the upstream side of a two-dimensional turret successfully reduced distortions at certain aperture pitch angles [2]. In another experiment, a spanwise array of synthetic jet actuators actively reduced flow fluctuations and delayed separation on a three-dimensional turret [3]. In an open-loop control experiment, synthetic jets were used to reduce the rms values of fluctuating velocity in the turbulent flow around a three-dimensional turret [4].

Closed-loop control systems are designed to improve performance over open-loop systems through robustness, the ability to compensate for uncertainties over a range of flight conditions, and by achieving more with less, reducing actuator power, size, and weight requirements. A closed-loop system used synthetic jets to delay the onset of stall on a NACA 4412 airfoil, consuming less power than an

open-loop system that increased stall angle by the same amount [5,6]. More recently, a proportional feedback controller was used to modulate synthetic jets on a three-dimensional turret and reduce fluctuation levels in the wake [7]. The tests were performed at Mach 0.3 in the Subsonic Aerodynamic Research Laboratory wind tunnel at Wright-Patterson Air Force Base.

Numerical analysis of steady suction around a turret demonstrated the advantages of employing suction as compared to other active flow control systems over a three-dimensional turret. This work found that steady suction is an effective control input to help delay separation and reduced the wake over the top of the turret [8].

Here, experimental active flow control tests have been performed with a three-dimensional turret at Mach 0.1 using suction as the control input. Compressible effects are not present at this speed, but systems for controlling velocity fluctuations in incompressible flows are assumed to be effective in controlling density fluctuations at higher speeds because of the strong correlation between velocity and density fluctuations [9]. Both open- and closed-loop control systems were implemented to reduce fluctuation levels over the aperture. For closed-loop control, a proportional-integrated controller employing a measurement and dynamical estimator was first developed computation demonstrated in [10].

II. Problem Description

The control problem involves fully turbulent, incompressible flow past a three-dimensional turret, and the control objective was to minimize levels of separation and velocity fluctuations above the aperture. Freestream conditions in the computational simulations and the wind-tunnel conditions in the experiment are approximately equal. The computational model of the turret and the wind-tunnel test article also match with some differences in the details, such as the turbulence in the freestream and the pitching parameters. The turret consisted of a 15.24-cm-diam (D) hemisphere mounted on a 15.24-cm-diam by 10.16-cm-high cylinder. The total height of the turret was $h = 17.76$ cm. These dimensions give the turret an aspect ratio of 1.2. A flat aperture, 7.112 cm in diameter, was located at the top of the turret. The top, hemispherical section could rotate within the cylindrical stand in two directions: pitch and yaw. Rotation about the pitch axis alone was examined here.

The pitch angle θ is defined as the angle between a vector normal to the aperture and the freestream vector as seen in right panel of Figure 1. When the normal is aligned with the turret centerline, the pitch angle is 90 deg. As the flat aperture pitches back, it becomes similar to a backward-facing ramp, separation levels increase as the pitch angle increases, and this increases levels of velocity fluctuations in the flow above and downstream of the aperture. The objective of the test was to manage and minimize the separation and concomitant fluctuations in the aperture field of view as the pitch angle was varied sinusoidally.

A closed-loop control system employed to alter the turbulent flow over the aperture was designed and evaluated in control-in-the-loop computational fluid dynamics simulations, as described in [10]. The measurement and dynamic estimator components of the closed-loop control system developed in the CFD simulations were calibrated with experimental data for the wind-tunnel flow control tests. The intent was not to use experimental data to validate CFD models and methods but rather to develop and evaluate closed-loop control designs for the wind tunnel through CFD simulations.

III. Experimental Test Configuration

The test facility at Syracuse University is a Gottingen-type, closed, recirculating tunnel in a horizontal configuration with continuously variable speeds of less than 4 m/s to approximately 70 m/s. For each test performed, the freestream velocity was set at 53 m/s, giving a Mach number 0.1. Thus, based on the diameter of the turret, Reynolds number is approximately 500,000. The test section is constructed of optical Plexiglas® with dimensions of $0.61 \times 0.61 \times 2.4$ m (width, height, length). The turret was mounted directly to the floor of the tunnel. A large data set of velocity were obtained by hot-wire measurements sampled at 10 kHz for 10 s at set vertical locations off the tunnel floor and 15.24 cm forward of the turret revealed that the incoming boundary-layer thickness was $\delta/h = 0.219$ based on the height of the turret, as seen in the left panel of Fig. 2. Hot-wire measurements were also taken 3.81 cm behind the leading edge of the turret at various elevations above the surface of the hemisphere along the centerline to obtain the boundary-layer thickness to be $\delta/h = 0.182$ over the turret, as seen in the right panel Fig. 2. The local Reynolds number Re_x varied linearly from 62,000 at $x/D = 0.1$ to 275,000 at $x/D = 0.5$ over the top of the hemisphere. See Figure 2.

The left panel of Fig. 1 contains a schematic of the top of the test article with the locations of the suction slots and the pressure transducers. Two concentric rings of suction jet slots circumscribe the aperture. Slots on one side of the centerplane were tied to a common manifold, and slots on the other were tied to another manifold. Each manifold was connected to a solenoid valve for dynamic flow control. A total of 30 acoustic ICP pressure transducers were located on and around the aperture. The pressure sensors have a resolution of 78 dB and a frequency bandwidth of 5 to 13 kHz. Surface pressure was sampled at a rate of 10 kHz using a National Instruments PXI-based 800 MHz signal conditioner with 24-bit, high-resolution A/D converters and an anti-aliasing filter.

Suction-jet velocity was controlled by cycling the suction valves at 25 Hz and modulating the duty cycle. From Fig. 3, the relationship between the coefficient of momentum and duty cycle is approximately linear between duty cycles of 30 and 90%. Velocity measurements were taken just above the slots using a hot-wire probe to determine the relationship between suction velocity and duty cycle. The Dantec PIV System measured two components of velocity

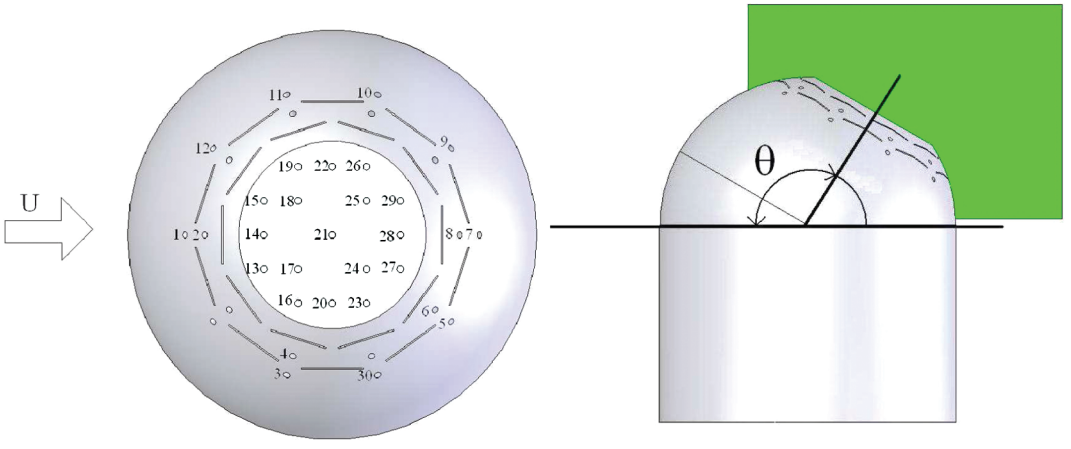

Fig. 1 A schematic of the top of the turret with sensor (left) and location of the PIV window (right). Jet slots are marked as lines and sensors as open circles.

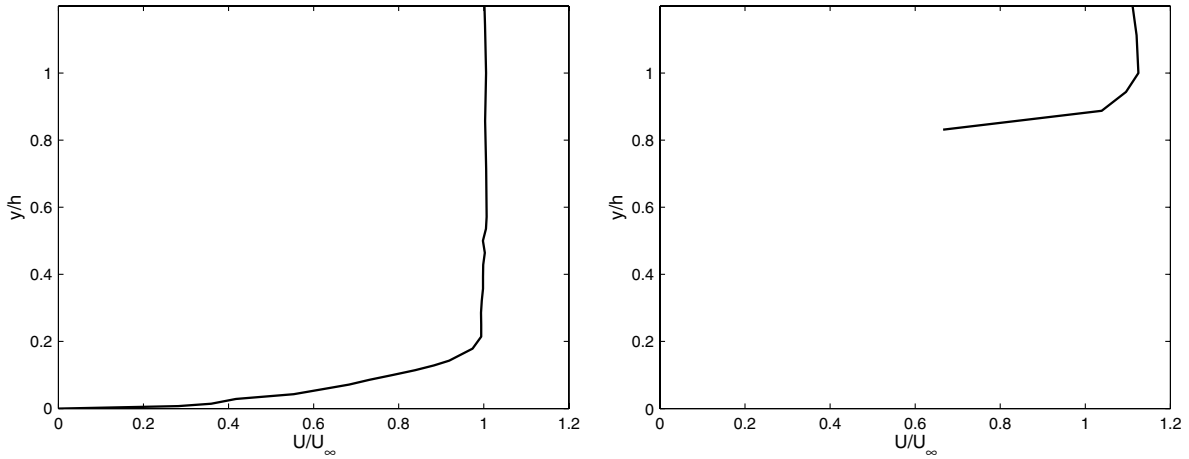

Fig. 2 The left panel shows the incoming boundary layer 15.24 cm ahead of the turret. The right panel shows the boundary layer over the surface of the turret, 3.81 cm behind the leading edge.

in the centerplane at a rate of 4 Hz using Dantec FlowMap software. The velocity measurements, surface pressure measurements, and suction valve duty cycle were phase aligned or synchronized in time.

Figure 4 contains photos of the mechanism that induces rotation about the pitch and yaw axes, housed under the turret. A drive shaft connected a stepper motor to the turret hemisphere through a gearing system, generating rotation about the pitch axis at the center of the hemisphere. The motor is rated to 58.61 N · cm of torque and was controlled by a National Instruments PXI 800 MHz signal conditioner with 24-bit, high-speed D/A converters.

IV. Static and Dynamic Pitching

The first series of wind-tunnel tests examined a set of static pitch angles between 110 and 130 deg at 5 deg increments conducted with no actuation. The purpose of examining various elevation angles was to determine a suitable dynamic pitch range where the flow goes from being attached to separated and back to attached without flow control. This pitch range allows for the ability to observe the intelligence of the closed-loop control to track the increase and decrease in velocity fluctuations through the rotation cycle of the hemisphere. The panels of Fig. 5 contain contours and streamlines of time-averaged velocity in the turret centerplane at static pitch angles of 110, 115, and 120 deg. At the pitch angle of 110 deg, the flow over the aperture is fully attached, but when the angle was increased to higher pitch angles the flow begins to separate from the aperture.

Note that the pitch angle of 115 deg marks the point of incipient separation with a stationary turret; flow was separated above the aperture in one run at this angle (shown here in Fig. 5b) and attached in another. This led to further investigations, where extensive measurements were made at 114 and 116 deg to examine the incipient nature of this region. At 114 deg, the flow was found to be always attached, whereas at 116 deg the flow was always separated, showing definitively that 115 deg is the incipient angle for these flow conditions.

Building upon the static pitching tests the next series of experiments examined a dynamically pitching turret. The aperture was rotated through a pitch range between two different flow regimes, attached to separated back to attached. Thus, the dynamic pitch range started at 110 deg, then rotated to 120 deg, and then back to 110 deg. The hemisphere of the turret was pitched dynamically in a sinusoidal matter using the following prescribed function:

$$\theta(t) = \left[115 - 5\cos\left(\frac{\omega}{\pi}t\right)\right]\frac{\pi}{180} \tag{1}$$

where $\omega = 2.4$ deg/s. Therefore, one pitching period was 8.3333 s. Again, velocity was sampled at 4 Hz and pressure at 10 kHz.

Figure 6 contains the mean velocity and fluctuating pressure results from the dynamic run with no actuation. The mean velocity data has been phase averaged over 102 pitching cycles. Comparing Figs. 6a–6c, the flow is attached as the pitch angle increases through 115 deg and detached as it decreases through 115 deg. In fact, when the angle increases, the flow remains attached until 119 deg, at which point it becomes massively separated. When the angle reaches the maximum of 120 deg and begins to decrease, the flow remains separated until 112 deg when it reattaches. The bottom-right panel of Fig. 6 contains centerline fluctuating-pressure time histories of the turret where the top time series (sensor 1) is the leading sensor and following time series are the subsequent sensors (sensors 14, 21, 28, and 7). The fluctuating-pressure amplitude ahead of the aperture (sensor 1 in Fig. 6d) increases as turret pitches back and the flow

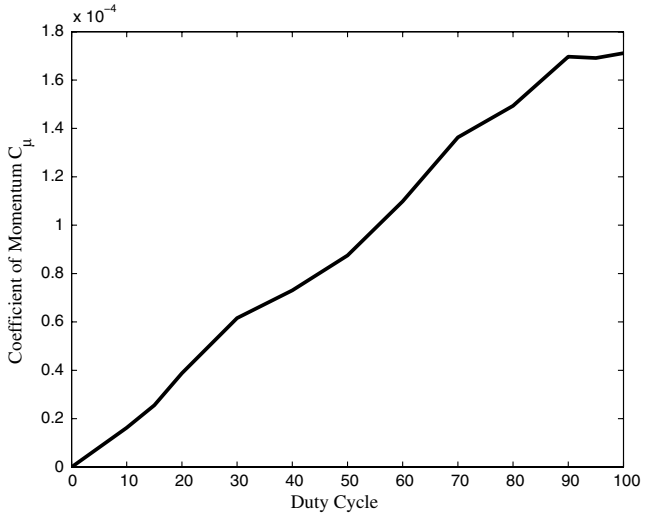

Fig. 3 Suction-jet coefficient of momentum vs suction-valve duty cycle.

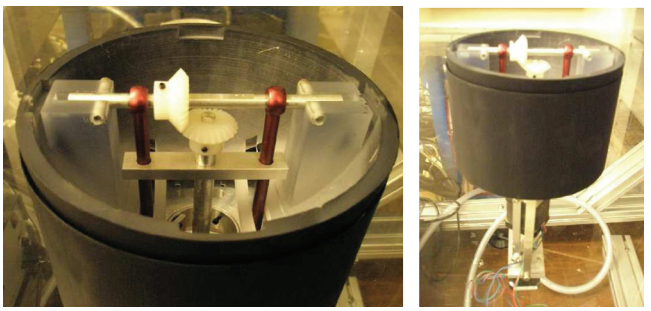

Fig. 4 Photos of the two-degrees-of-freedom rotational mechanism housed inside the turret.

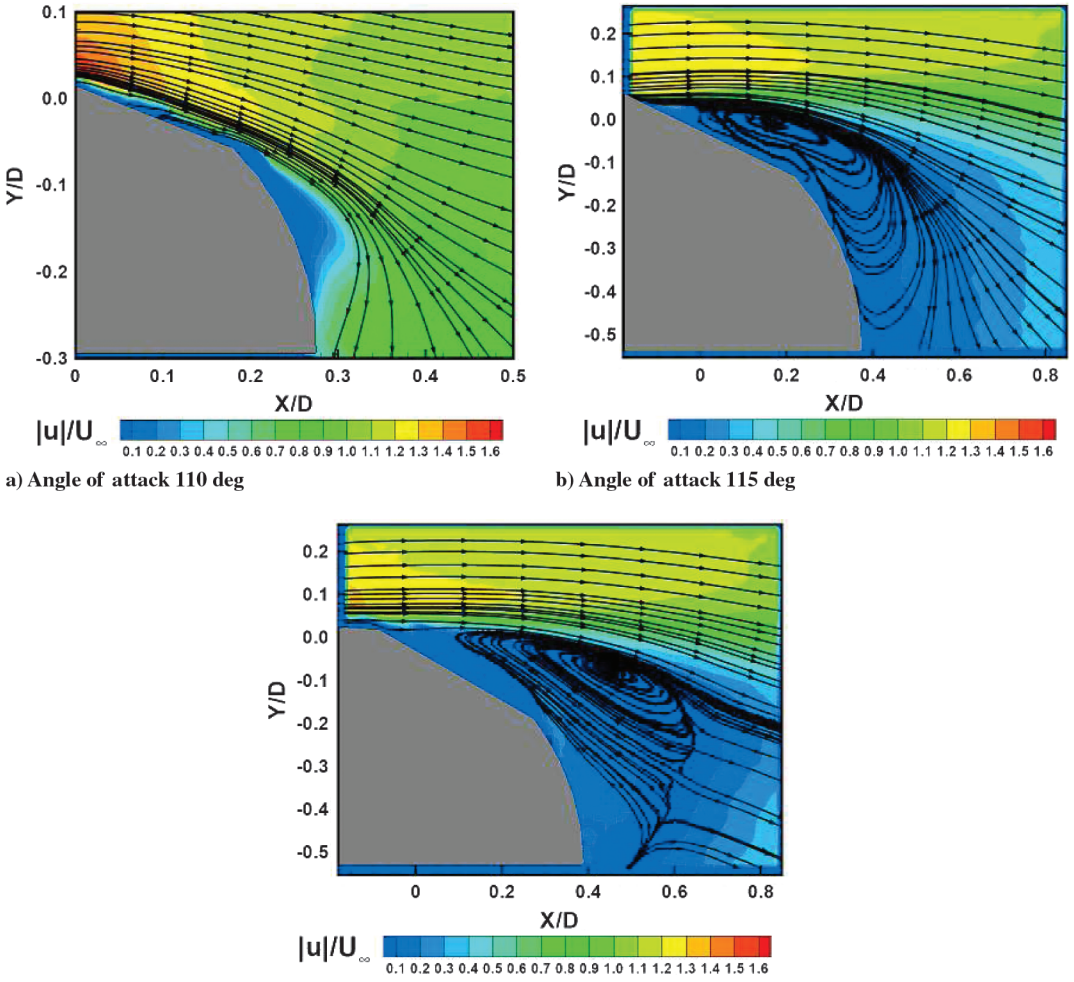

a) Angle of attack 110 deg

b) Angle of attack 115 deg

c) Angle of attack 120 deg

Fig. 5 Contours and streamlines of time-averaged velocity on the PIV centerplane for three pitch angles with no suction jet actuation.

separates. However, the sensors located on and downstream of the aperture (sensors 14, 21, 28, and 7 in the lower four time series) exhibit an opposite trend: fluctuating pressure amplitude decreases as the flow separates, indicating stall over the aperture. Comparing results from the static and dynamic runs reveals that the influence of rotation produces a strong hysteresis with the flow above the aperture even when the pitching rate is modest with respect to the time scales of the flow.

Open-loop flow control runs were executed with a pitching turret and steady suction at 30, 50, 70, and 90% duty cycles. Figure 7 contains results from the dynamic run at 50% duty cycle. Again, the velocity data were phase averaged over 102 pitching cycles and the pressure data are instantaneous. From the panels containing velocity contours and streamlines, steady suction at the 50% duty-cycle level moves the separated flow downstream and below the aperture. Comparing the fluctuating-pressure time series of Figs. 6d and 7d, steady suction, and the elimination of separation above the aperture that results, actually increases amplitude of the fluctuations in all but sensor 1, which is the only sensor located upstream of the jet slots. Root-mean-square values of fluctuating surface pressures are higher than baseline values in all of the open-loop runs (for all of the sensors but sensor 1). The same trend was confirmed at a duty cycle of 100% (valves fully open), eliminating transmission of vibrations from the valves as a possible source of the trend.

V. Initial Closed-Loop Control Run

The fluctuating-pressure time series of the dynamic pitching with no flow control, seen in Fig. 6d, shows that sensor 1's (top panel) fluctuating surface pressure amplitude increases as the hemisphere rotates towards the extreme pitch angle of 120 deg and decreases when the hemisphere rotates in the opposite direction. The level of velocity fluctuations over the aperture has a trend similar to the amplitude of the fluctuating surface pressure during the pitch cycle where, as the hemisphere pitches backward, the velocity fluctuations increase, then the fluctuation levels decrease pitching forward. For an initial closed-loop control, a simple proportional controller was employed using the signal from sensor 1 as the feedback signal. The control objective was to minimize fluctuations in the single-sensor pressure measurement while using suction as the control input. The duty cycle of the suction valve was modulated by the controller. Like the previous runs, the turret was pitched at a rate of $\omega = 2.4$ deg/s between 110 and 120 deg according to the function in Eq. (1) for a total of 102 pitch cycles. All of the 20 jet slots were activated, operating as a single unit in each closed-loop control case.

Four control runs were executed using four different digital pressure filters. The digital filters include a band-pass filter in the range of 30 to 500 Hz, a band-stop filter in the range of 0 to 8 Hz ∪ 12 to 500 Hz, a low-pass filter in the range of 0 to 500 Hz, and a very-low-pass filter in the range of 0 to 8 Hz.

Performance output is defined as

$$u_{\text{rms}}(t) \equiv \sqrt{\frac{1}{N_{\text{PIV}}}\left(\sum_{i=1}^{N_{\text{PIV}}}\{[u_1(\boldsymbol{x}_i,t)-\bar{u}_1(\boldsymbol{x}_i)]^2+[u_2(\boldsymbol{x}_i,t)-\bar{u}_2(\boldsymbol{x}_i)]^2\}\right)} \quad (2)$$

where $u_{1,2}(\boldsymbol{x}_i, t)$ are the instantaneous velocities in the centerplane, and $\bar{u}_{1,2}(\boldsymbol{x}_i)$ are the mean (time-averaged) velocities averaged, where

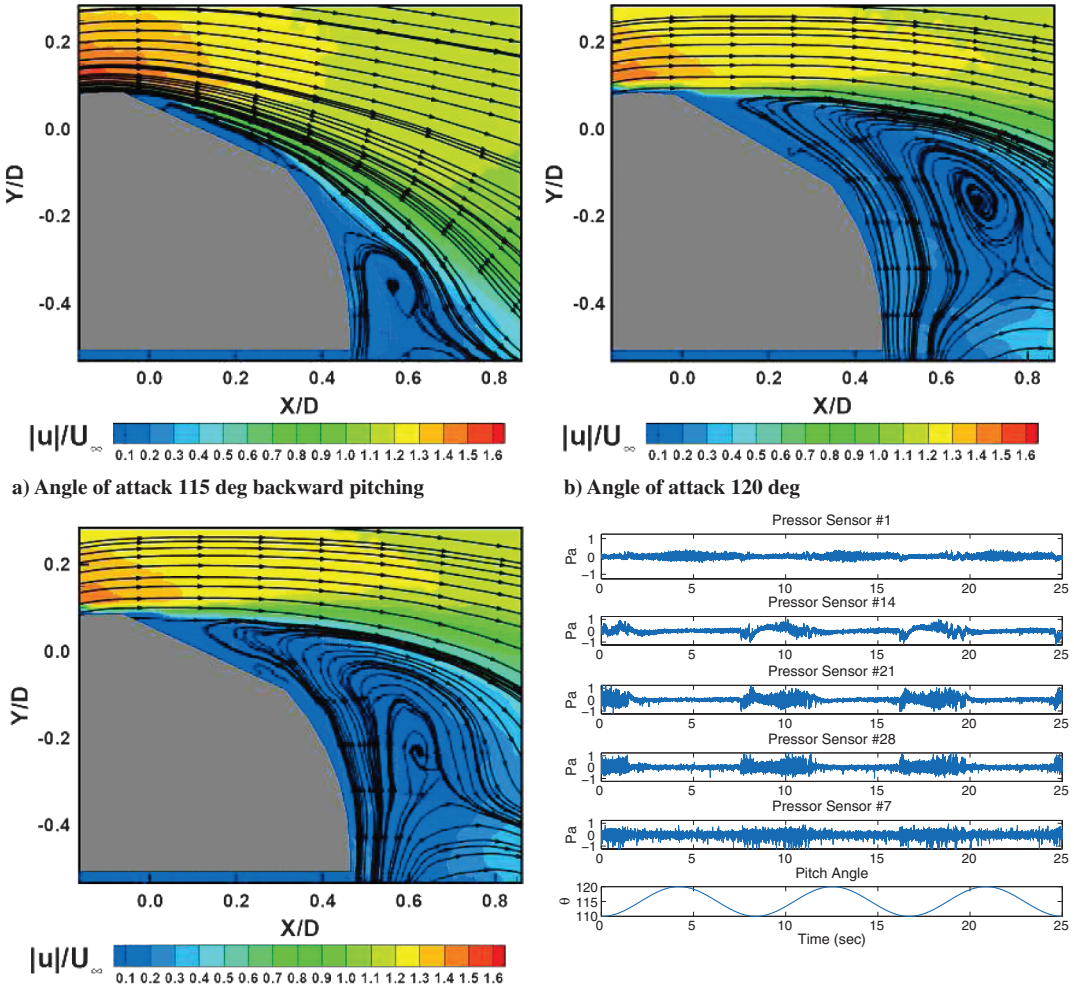

a) Angle of attack 115 deg backward pitching

b) Angle of attack 120 deg

c) Angle of attack 115 deg forward pitching

d) Fluctuating pressure time series

Fig. 6 Velocity contours and streamlines in the PIV centerplane from the run with dynamic pitching and no actuation at dynamic pitch angles of 115 deg (increasing) in the top-left panel, 120 deg in the top-right panel, and 115 deg (decreasing) in the bottom-left panel. Time histories of five surface pressures on the turret centerline from the dynamic run in the bottom-right panel.

$N_{\mathrm{PIV}} = 3400$ PIV snapshots. N_{PIV} is the number of PIV-sampled points on the centerplane.

The results are summarized in Table 1. The column labeled "$\langle DC \rangle$, %" contains time-averaged values of the jet duty cycle. Values in the right-most column are measures of control effectiveness or efficiency (the ratio of fluctuating velocity reduction to required control input):

$$\xi = \left| \frac{\langle u_{\mathrm{rms}} \rangle_{\mathrm{Control}} - \langle u_{\mathrm{rms}} \rangle_{\mathrm{No\ Control}}}{\langle DC \rangle} \right| \tag{3}$$

The efficiency term (ξ) has a ± 0.0004 $(\mathrm{m/s})/DC$ uncertainty value. Higher values of ξ correspond to more efficient controllers. Two of the simple closed-loop controllers reduced velocity fluctuations more than the representative open-loop case (50% duty cycle). Based on the ratio ξ in the right-most column of the table, all of the closed-loop controllers operated more efficiently than the open-loop system. The runs with the band-pass and low-pass filters performed most efficiently, and data from the run with the band-pass filter were used to construct an advanced controller.

Figure 8 compares results from the band-pass-filtered closed-loop run, an open-loop run, and the baseline run with no control jets averaged over 34 sets of three pitching cycles: time histories of performance output (rms values of fluctuating velocity) and control input (jet momentum coefficient). From mean velocity averaged over 102 pitching cycles, seen in Figs. 9a–9c, the separation region was moved aft of and below the aperture by the initial closed-loop controller as compared to the open-loop controller.

VI. Controller Design

Data obtained from the initial closed-loop run were used to construct an advanced controller that employed a dynamical estimator coupled with a Kalman filter. The advanced controller was designed using Clear Science Corporation's software SMARTFLOW, which is described in detail in [10]. The control objective in the initial runs was to minimize pressure fluctuations from the single pressure sensor, but the true objective was to minimize velocity fluctuations (u_{rms}) in the aperture field of view.

A more robust controller would use both velocity measurements and multiple pressure sensors by relying on a general pressure-velocity correlation contained within the measurement-based estimator rather than any specific relationship between surface pressures and velocity. The velocity measurements taken with the PIV at a rate of 4 Hz were used to construct the measurement and dynamic estimators as well to evaluate controller performance. Although the velocity measurements were not time-resolved, the strong correlation between velocity and pressure [5] allows for a time-resolved measurement to further enrich the velocity data set. The single pressure sensor used in the initial closed-loop runs was chosen because it correlated well with pitch angle: pressure variance increased as the angle (and extent of flow separation) increased. The correlation seems to be due primarily to the sensor's location upstream of the jet slots, which will change as the yaw angle changes. The measurement-based estimator in the more advanced controller used 18 sensors: sensors 1, 2, 3, 5, 6, 8, 11, 12, 13, 14, 15, 16, 17, 18, 25, 26, 29, and 30, identified in the right panel of Fig. 1. These

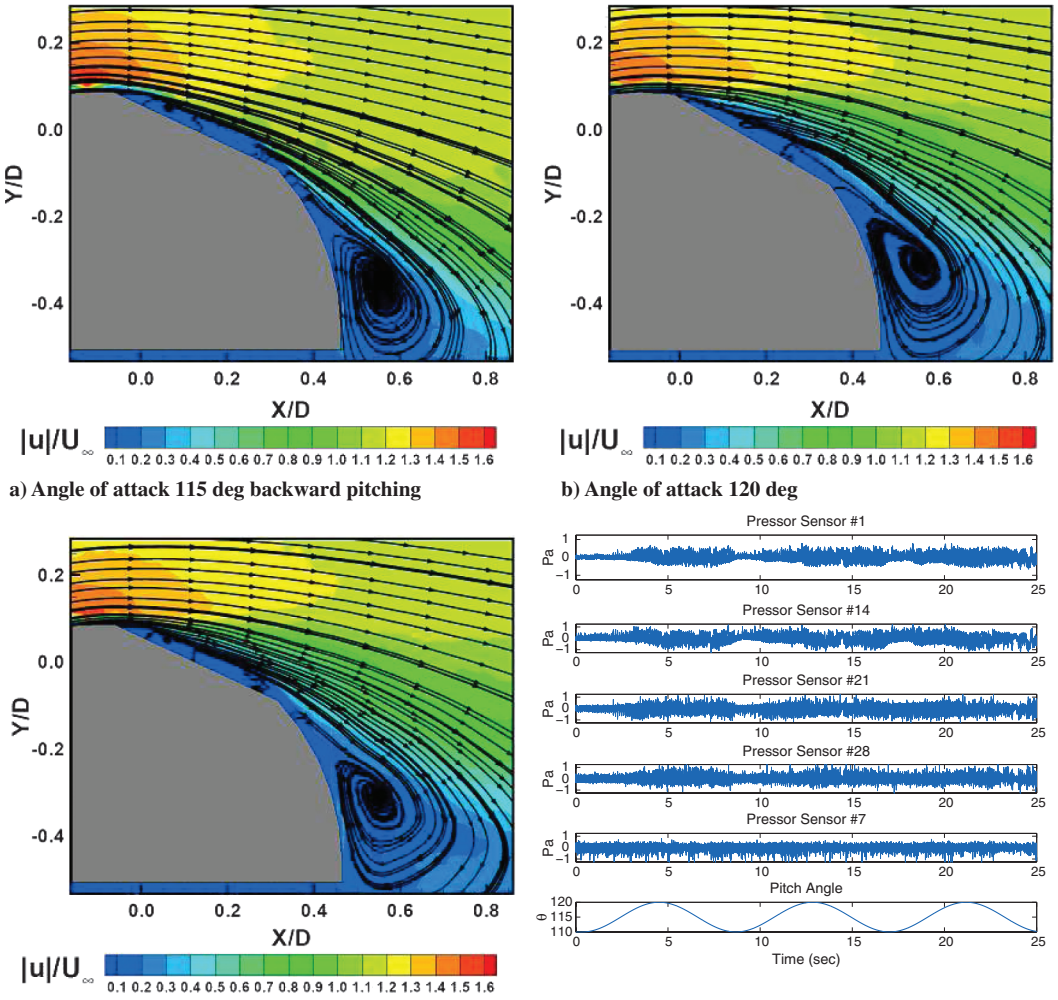

Fig. 7 Velocity contours and streamlines in the PIV centerplane from the run with dynamic pitching and open-loop control (50% duty cycle) at dynamic pitch angles of 115 deg (increasing) in the top-left panel, 120 deg in the top-right panel, and 115 deg (decreasing) in the bottom-left panel. Time histories of five surface pressures on the turret centerline from the dynamic run in the bottom-right panel.

sensors were chosen because of their high correlation between pressure signal and velocity field observed during construction of the measurement and dynamic estimators relative to each other. Pressure sensors that are located on the aperture itself for the purpose of investigating the flows and developing the preliminary controllers; however, these sensors would interfere with operation in real optical applications, and final designs would exclude them.

A. Controller Plant

The first step in constructing estimators was to compute a set of proper orthogonal decomposition (POD) basis functions using PIV snapshots. The left panel of Fig. 10 contains the POD energy distributions in the reduced-order model (ROM) built with snapshots obtained from the initial closed-loop run. Four POD modes contain more than 80% of the perturbation energy, and this number of modes is chosen for the estimators. The right panel of Fig. 10 contains comparisons of time histories of rms velocity fluctuations averaged over 34 sets of three pitching cycles from the PIV data (labeled as "RAW") and time histories obtained by projecting the PIV snapshots onto the four POD modes: $u_{\text{rms}}(t) \approx \sqrt{a_{(n)}(t)a_{(n)}(t)}$, $n = 1, 4$. Even with only four modes in the models, the approximations based on projections are very accurate.

Table 1 Summary of results from the wind-tunnel runs; ξ is defined in Eq. (3) and is a measure of controller efficiency

Run description	$\langle u_{\text{rms}} \rangle$	$\langle DC \rangle$, %	ξ
No control	9.65		
Open-loop control	4.14	50	0.11
Closed-loop control (band-pass)	4.67	33	0.15
Closed-loop control (band-stop)	3.86	44	0.13
Closed-loop control (low-pass)	3.47	42	0.15
Closed-loop control (very-low-pass)	5.14	35	0.13

The linear measurement-based estimator was constructed by employing the modified linear stochastic measurement [11–13]. The estimated POD coefficients are expanded with a Taylor series expansion, and the higher-order terms are truncated to yield Eq. (4):

$$\tilde{a}_{(n)}(t) \approx B_{(ni)} p_{(i)}(t) \tag{4}$$

where $B_{(ni)}$ represents the measurement-based estimates of the POD coefficients that approximate the instantaneous perturbation velocity ($\tilde{u}^i(x,t)$):

$$\tilde{u}^i(x,t) \approx \tilde{a}_{(n)}(t)\phi^i_{(n)}(x) \tag{5}$$

The dynamical estimator consists of a set of ordinary differential equations (ODEs) that describes the flow over the aperture, including the control input and hemisphere rotation. The ODEs are constructed by projecting the momentum conservation equation onto the POD basis. The dynamical estimator is then linearized by excluding the bilinear terms within the system, yielding Eq. (6):

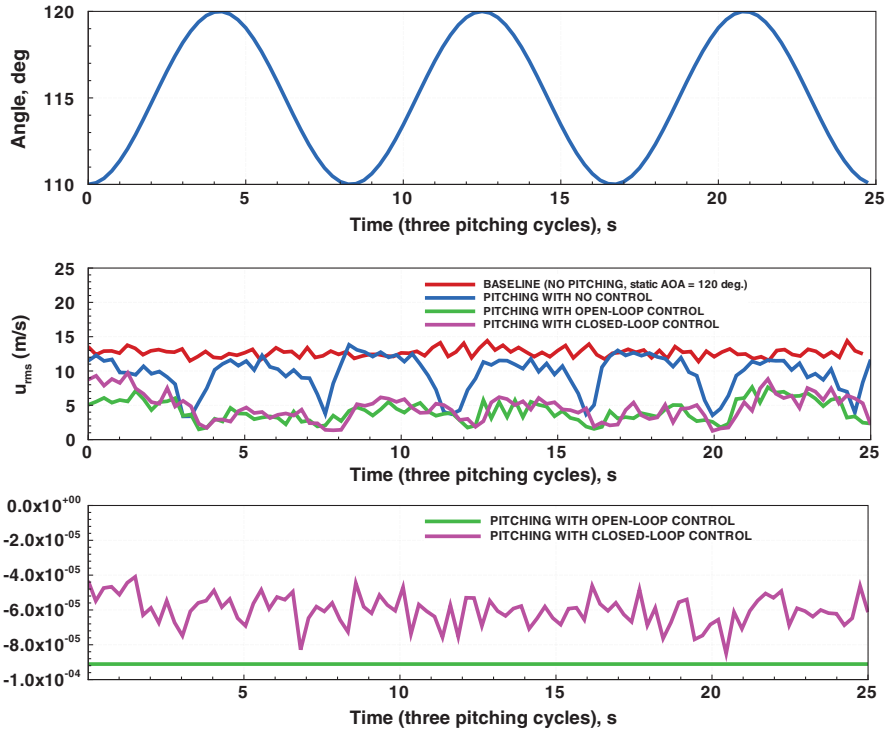

Fig. 8 Comparisons of the baseline (no control), open-loop control, and initial closed-loop control runs.

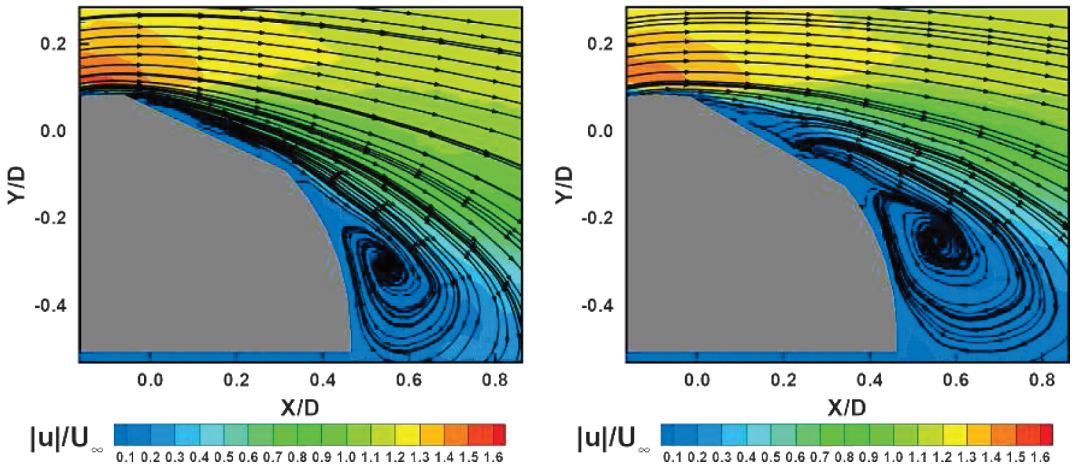

a) Angle of attack 115 deg backward pitching

b) Angle of attack 120 deg

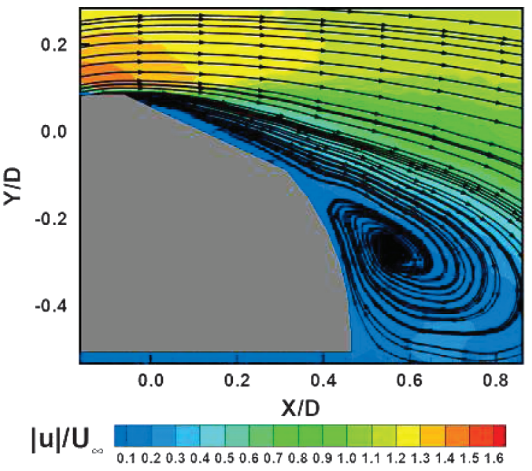

c) Angle of attack 115 deg forward pitching

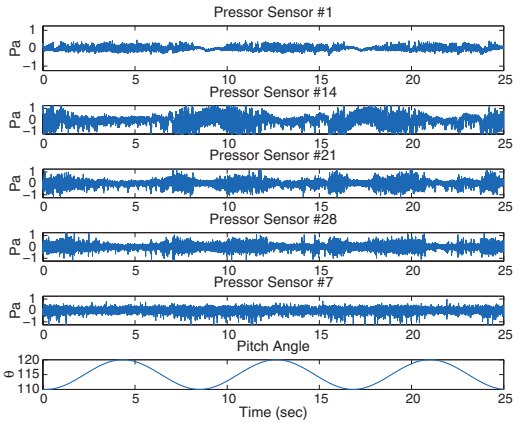

d) Fluctuating pressure time series

Fig. 9 Velocity contours and streamlines in the PIV centerplane from the run with dynamic pitching and simple closed-loop control (band-pass) at dynamic pitch angles of 115 deg (increasing) in the top-left panel, 120 deg in the top-right panel, and 115 deg (decreasing) in the bottom-left panel. Time histories of five surface pressures on the turret centerline from the dynamic run in the bottom-right panel.

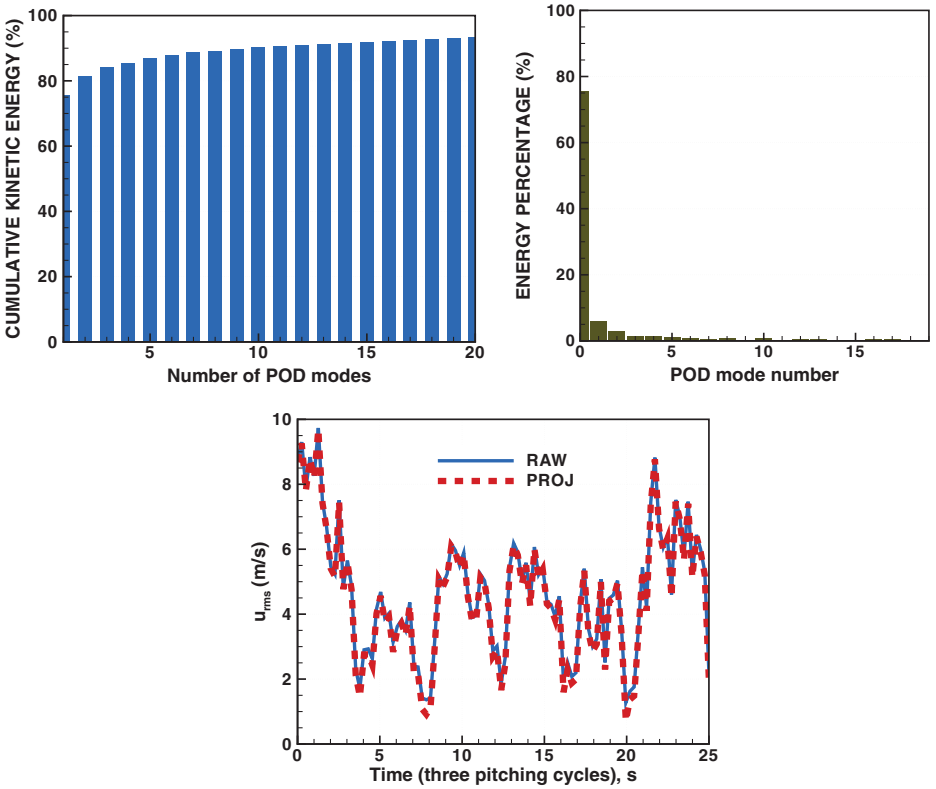

Fig. 10 Energy distribution in the POD-based ROM (left). Energy percentage of individual POD modes (bottom). Time histories of u_{rms} from the PIV data (RAW) and approximations obtained by projecting the PIV snapshots onto the first four modes in the model, labeled "PROJ" (right).

$$\dot{\hat{\mathbf{x}}} = \mathbf{a}_0 + \mathbf{A}_1\hat{\mathbf{x}} + \mathbf{b}_0 u + \mathbf{b}_2\dot{u} + \mathbf{b}_3\dot{\eta} + \mathbf{b}_4\ddot{\eta} \tag{6}$$

where $\hat{\mathbf{x}}$ are the POD coefficients, u corresponds to the control input, and $\dot{\eta}$ represents the rotation of the hemisphere. The exclusion of the bilinear terms allows the dynamical estimator to be easily solved. The bold lowercase letters denote vectors, whereas the bold uppercase letters denote matrices, and the coefficients $\mathbf{a}_0$, $\mathbf{A}_1$, $\mathbf{b}_0$, $\mathbf{b}_2$, $\mathbf{b}_3$, and $\mathbf{b}_4$ are solved during the projection of the conservation equation.

Figure 11 contains time histories of the POD coefficients from the dynamical estimators (D-ESTs), the measurement-based estimators (M-ESTs), along with the values obtained by projecting the PIV

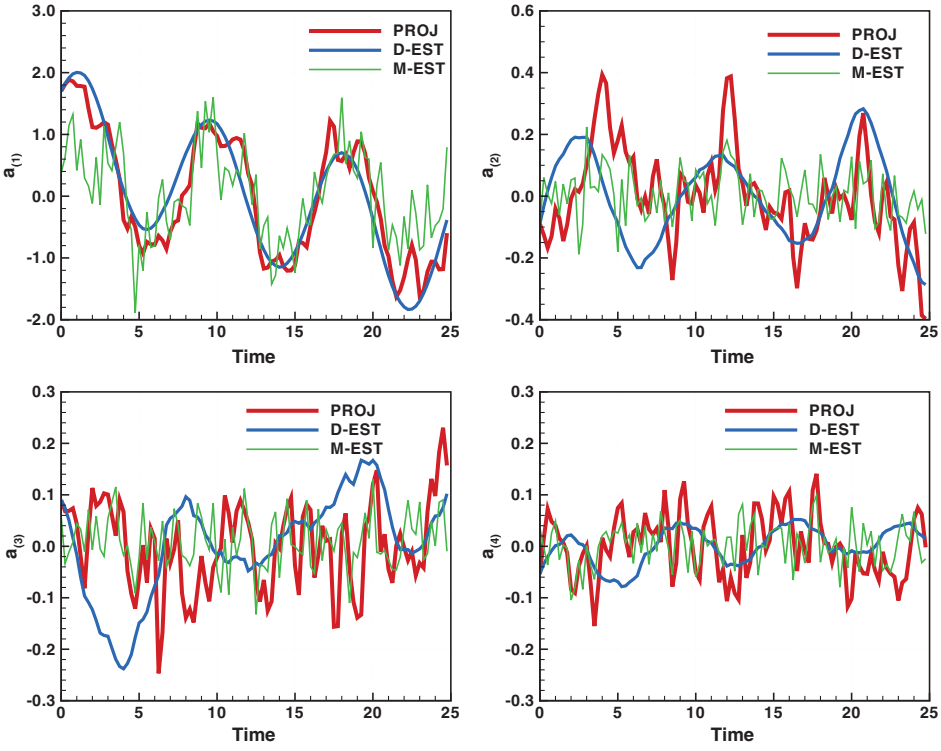

Fig. 11 Time histories of the first four POD coefficients from the D-ESTs and M-ESTs as well as values obtained by projecting the PIV snapshots onto the four POD modes of the model (PROJ).

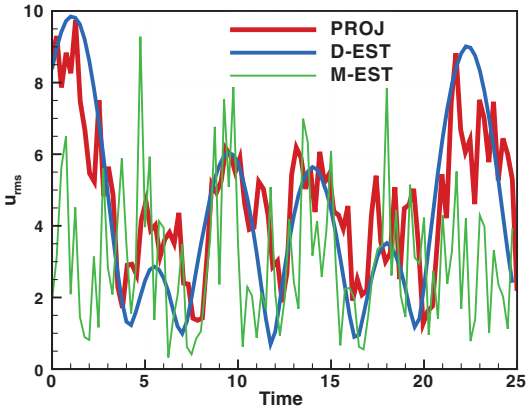

Fig. 12 Approximations of u_{rms} from the D-ESTs and M-ESTs as well as values obtained from projected POD coefficients (PROJ).

snapshots onto the four POD modes averaged over 34 sets of three pitching cycles. From the top-left panel of the Fig. 11, predictions from both types of estimator are accurate in predicting the trends in the first POD coefficient, and this mode contains more than 75% of the perturbation energy. Note how much less noise there is in the dynamical state estimates than in the measurement-based state estimates. This was exploited with the Kalman filter.

The Kalman filter is combined with the dynamical estimator in Eq. (7):

$$\dot{\hat{\mathbf{x}}} = \mathbf{a}_0 + \mathbf{A}_1\hat{\mathbf{x}} + \mathbf{b}_0 u + \mathbf{b}_2\dot{u} + \mathbf{b}_3\dot{\eta} + \mathbf{b}_4\ddot{\eta} + \mathbf{K}_f(\hat{\mathbf{x}}_m - \mathbf{H}\hat{\mathbf{x}}) \quad (7)$$

where $\mathbf{K}_f$ is the Kalman filter gain, unity matrix $\mathbf{H}$ is the sensitivity term, and $\hat{\mathbf{x}}_m$ is the measurement-based state estimate. The Kalman gain is defined as

$$\mathbf{K}_f = \mathbf{P}\mathbf{H}^T\mathbf{V}_s^{-1} \quad (8)$$

where the power spectral density of the error ($\mathbf{V}_s$) in measurement-based state estimates is defined in Eq. (9):

Table 2 Parameter settings for the wind-tunnel control runs

Quantity	Symbol	Run 1	Run 2	Run 3
Signal-to-noise ratio	SNR	5.0	5.0	5.0
Process covariance	W_p	3.3×10^{-1}	3.3×10^{-4}	3.3×10^{-7}
Measurement covariance	V_p	3.3×10^{-4}	3.3×10^{-4}	3.3×10^{-4}

$$\mathbf{V}_s = \mathbf{B}\mathbf{D}_Z\mathbf{V}\mathbf{D}_Z\mathbf{B}^T \quad (9)$$

The covariance of the measurement-based and dynamical estimates (P) is calculated using the Riccati equation,

$$\dot{\mathbf{P}} = \mathbf{A}_1\mathbf{P} + \mathbf{P}\mathbf{A}_1^T + \mathbf{W} - \mathbf{P}\mathbf{H}^T\mathbf{V}_S^{\dagger}\mathbf{H}\mathbf{P} \quad (10)$$

The power spectral density of the measurement noise is represented as $\mathbf{V} = V_p\mathbf{I}$, whereas the process-noise power spectral density of the modeling uncertainties is represented as $\mathbf{W} = W_p\mathbf{I}$.

B. Regulator

As stated previously, the control objective in the wind-tunnel experiment was to minimize velocity fluctuations in the aperture field of view (or at least over the area of intersection between the PIV window and field of view). Figure 12 contains approximations of u_{rms} from the dynamical and measurement-based estimators, along with values from the projected POD coefficients averaged over 34 sets of three pitching cycles. From Fig. 12, the dynamical estimator was able to accurately track the velocity fluctuations. The measurement-based estimator exhibits relatively high noise levels, even when the pressure signals are filtered, but the dynamical estimator and Kalman filter were designed to address this issue.

An initial proportional-integral (PI) controller was developed in computational tests [10] to reduce the integrated shear stress y over the aperture of the turret,

$$u(t) = K_1[y(t) - y_T] + K_2\int_0^t [y(\tau) - y_T]\,\mathrm{d}\tau \quad (11)$$

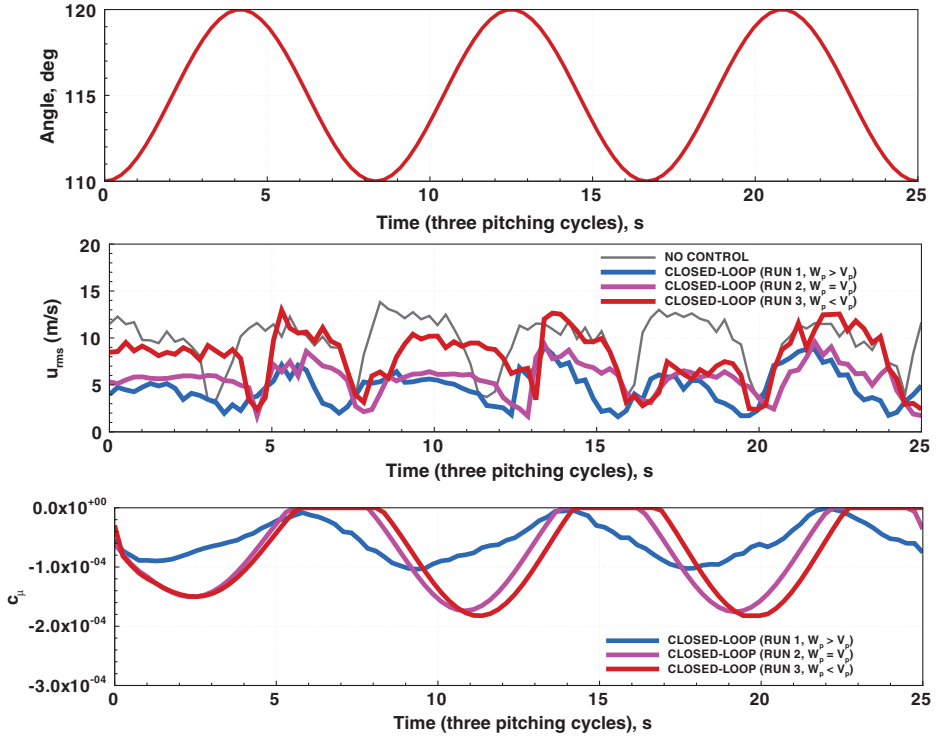

Fig. 13 Comparison of pitching runs with and without control: results from the new controller.

Table 3 Summary of results from the wind-tunnel runs with open- and closed-loop control; ξ in the right-most column is defined in Eq. (3) and is a measure of control efficiency, the ratio of fluctuating velocity reduction to required suction; the efficiency term ξ has a ± 0.0004 (m/s)/DC uncertainty value

Run description	$\langle u_{\text{rms}} \rangle$	$\langle DC \rangle$, %	ξ
No control	9.65		
Open-loop control	4.14	50	0.11
Simple closed-loop control (band-pass)	4.67	33	0.15
Advanced closed-loop control (run 1, $W_p > V_p$)	4.69	30	0.17
Advanced closed-loop control (run 2, $W_p = V_p$)	5.64	40	0.10
Advanced closed-loop control (run 3, $W_p < V_p$)	7.97	41	0.04

where K_1 and K_2 are the proportional and integral gains, respectively. With performance output defined as spatially integrated values of $u_{\text{rms}}(t)$, the controller used approximations from the estimators, and the PI regulator in Eq. (11) becomes

$$\dot{u} = k_1(\sqrt{\hat{x}_n(t)\hat{x}_n(t)} - 0) + k_2 \int_0^t (\sqrt{\hat{x}_n(\tau)\hat{x}_n(\tau)} - 0)\,\mathrm{d}\tau \quad (12)$$

where u is the suction-valve duty-cycle percentage, and the objective was to reduce fluctuating velocity to zero. The gains $k_{1,2}$ are determined heuristically, which can be a time-consuming process involving a number of wind-tunnel runs. Alternatively, a linear quadratic regulator (LQR) automatically determines gains that minimize the following cost function:

$$J \equiv \frac{1}{T}\int_0^T (\hat{x}_n\hat{x}_n + r\dot{u}^2)\,\mathrm{d}t \quad (13)$$

The parameter r weights the penalty assigned to the control input ($\dot{u}$).

Next, the dynamical estimator from Eq. (6) is written as

$$\dot{\hat{\boldsymbol{x}}} = \boldsymbol{a}_0 + \boldsymbol{A}_1\hat{\boldsymbol{x}} + \boldsymbol{b}_0 u + \boldsymbol{b}_2\dot{u} + \boldsymbol{C}\boldsymbol{w} \quad \text{and} \quad \dot{\boldsymbol{w}} = \boldsymbol{H}\boldsymbol{w} \quad (14)$$

where

$$\boldsymbol{C} = (\,\boldsymbol{b}_3 \quad \boldsymbol{b}_4\,), \qquad \boldsymbol{w} = (\dot{\eta}, \ddot{\eta})^T, \quad \text{and} \quad \boldsymbol{H} = \begin{pmatrix} 0 & 1 \\ -\omega^2 & 0 \end{pmatrix} \quad (15)$$

where ω is the pitching frequency, defined in Eq. (1). Defining an augmented state estimate as $\boldsymbol{z} \equiv (\hat{\boldsymbol{x}}, u, \boldsymbol{w})^T$ and minimizing the cost function in Eq. (13) produces the following control law:

$$\dot{u} = -K_m^{\text{LQR}} z_m \quad (16)$$

The dynamical estimator without the Kalman filter was imported from SMARTFLOW into Matlab, and the following gains were computed:

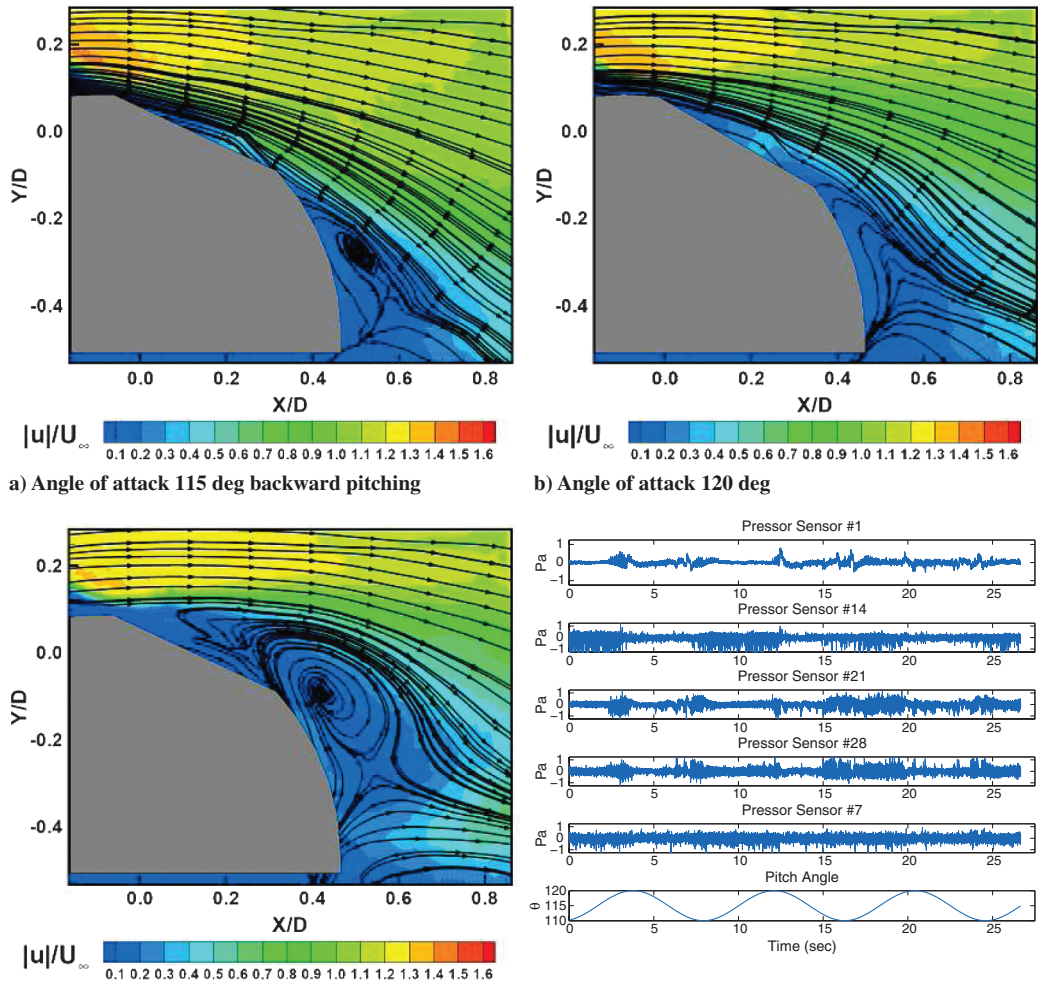

a) Angle of attack 115 deg backward pitching

b) Angle of attack 120 deg

c) Angle of attack 115 deg forward pitching

d) Fluctuating pressure time series

Fig. 14 Velocity contours and streamlines in the PIV centerplane from the run with dynamic pitching and advanced closed-loop control (run 1) at dynamic pitch angles of 115 deg (increasing) in the top-left panel, 120 deg in the top-right panel, and 115 deg (decreasing) in the bottom-left panel. Time histories of five surface pressures on the turret centerline from the dynamic run in the bottom-right panel.

$$\boldsymbol{K}^{\mathrm{LQR}} = (\,-0.2746 \quad 0.5013 \quad 0.0482 \quad -0.0949 \quad 0.0064 \quad -1.3309 \quad -3.2540\,)^T \times 10^3 \tag{17}$$

The gains in Eq. (17) were computed after reducing the weighting factor r in Eq. (13) to its lowest possible value, which effectively imposed no penalty on the control input.

VII. Closed-Loop Control Run with an Advanced Controller

Three compensators (LQR regulators with Kalman filters) were designed using three different values of the process covariance, whereas the measurement error covariance V_p was set to 3.3×10^{-4}. As the process covariance W_p decreased, the controller relied more on the dynamical estimator and less on the measurement-based estimator. From Table 2, the process covariance is highest in run 1 and lowest in run 3.

Figure 13 contains time histories of fluctuating velocity (middle panel) and jet-momentum coefficient (bottom panel) from the three control runs, along with baseline histories from the uncontrolled run averaged over 34 sets of three pitching cycles. Comparing the blue, pink, and red curves in the middle panel, it is clear that heavy reliance on the dynamical estimator results in poorer performance. The best control is achieved in run 1, where the measurement-based estimator dominates. From the pink and red curves in the bottom panel of Fig. 13, the Kalman filter reduces noise in the control input significantly when the dynamical estimator is heavily weighted; however, the blue curve indicates that substantial filtering is effected even in run 1 when the dynamical estimator is weighted much less: compare the relatively smooth blue curve in the bottom panel of Fig. 13 with the noisy pink curve in the bottom panel of Fig. 8. Comparison between the middle panel and the top panel in Fig. 13 shows a phase shift of the pitch angle and the u_{rms} in each control case. The phase shift of the u_{rms} for the no-control case indicates that a hysteresis of the flow develops over the turret due to the rotation of the hemisphere. This phase shift propagates to the control cases with varying amounts, depending on the amount of measurement and process covariance of the dynamical estimator.

From the bottom panel of Fig. 13, the control input modulates with pitch angle in all three runs with the advanced controllers. The phase shift between pitch angle and input varies between the three runs, but the turret motion is clearly driving the input, and modulation in the jet amplitude is not small. Conversely, the pink curve in the bottom panel of Fig. 8 indicates little or no correlation between control input from the simpler controller and pitch angle: modulations in the jet momentum coefficient are essentially random.

Table 3 summarizes results from the various runs: time-averaged values of fluctuating velocity, control input $\langle DC \rangle$, and controller efficiency ξ, defined in Eq. (3). The time-averaged velocity at various pitch angles for run 1 is seen in Figs. 14a–14c, as well as the centerline fluctuating surface pressure. Higher values of ξ correspond to more efficient controllers. Again, the run with a steady suction jet operating at 50% duty cycle is chosen as the representative open-loop case. It effects the largest reduction in fluctuating velocity (57%); however, it is significantly less efficient than the two most efficient closed-loop controllers. The most efficient simple controller (band-pass) reduces fluctuating velocity by 52% and the most efficient advanced controller (run 1) by 51%. Comparing the bottom-left panels of Figs. 7, 9, and 14, separated flow is, on average, closer to the aperture at a pitch angle of 115 deg (decreasing) in the advanced-controller run (run 1) than it is in the open-loop and simple closed-loop control runs, reflecting the slightly higher time-averaged fluctuating velocity in the advanced-controller run.

Comparing the bottom-right panels of Figs. 7, 9, and 14, the behavior of fluctuating pressures from the five sensors on the turret centerline is qualitatively similar in the open-loop, simple closed-loop, and advanced closed-loop runs. From the values of ξ in Table 3, the advanced controller in run 1 is 13% more efficient than the most efficient simple controller and 55% more efficient than open-loop control.

VIII. Conclusions

Above the aperture of the turret, the complexity of the flow increased significantly due to the pitching of the hemisphere. As the hemisphere pitched through its cycle, the flow over the aperture experienced various flow states. Separation and turbulence levels in the flow are altered by employing suction as the control input. Using suction with either open-loop or closed-loop control effectively delayed the onset of separation and, when separation did occur, the levels of turbulence over aperture were reduced. Although the open-loop control was effective at reducing the levels of separation, it was not as efficient as some of the closed-loop control cases.

Closed-loop systems for controlling flow separation and turbulence above a pitching turret have been developed and tested through a series of control-in-the-loop CFD simulations and wind-tunnel runs. Levels of flow separation and turbulence change as the turret pitches, and the systems successfully reduce these levels in the dynamic environment through feedback control, meeting the objective of control in the presence of disturbances over a range of operating conditions. Another objective was the minimization of control input: achieving threshold levels of control with less actuator energy. Closed-loop systems in the wind-tunnel runs are as much as 55% more efficient than a representative open-loop system as measured by the ratio of reduction in fluctuating velocity to required control input.

The efficiency of the controller seems to be sensitive to the control signal. The initial simple closed-loop controller showed that the control cases that allowed the higher frequencies to pass through had the most significant reduction of the turbulence levels and higher efficiency. The advanced controller case in which the measurement estimator was emphasized (run 1) also performed more efficiently due to the incorporation of the higher frequencies. Thus, both controllers captured more of the turbulence within the flow than the other controller that did not perform as well.

Acknowledgments

This material is based upon work supported by Clear Science Corp. and the U.S. Air Force Research Laboratory's Air Vehicles Directorate under contract FA8650-08-C-3827 and grant FA9550-09-1-0051. Any opinions, findings, conclusions, or recommendations expressed in the material are those of the authors and do not necessarily reflect the views of the U.S. Air Force.

References

[1] Nightingale, A. M., Goodwine, B., Lemmon, M., and Jumper, E. J., "'Feedforward' Adaptive-Optic System Identification Analysis for Mitigating Aero-Optic Disturbances," 38th AIAA Plasmadynamics and Lasers Conference, Miami, FL, AIAA Paper 2007-4013, June 2007.

[2] Gordeyev, S., T. E. Hayden, and Jumper, E. J., "Aero-Optical and Flow Measurements Over a Flat-Windowed Turret," *AIAA Journal*, Vol. 45, No. 2, 2007, pp. 347–357. doi:10.2514/1.24468

[3] Vukasinovic, B., and Glezer, A., "Control of a Separating Flow over a Turret," 37th AIAA Fluid Dynamics Conference, Miami, FL, AIAA Paper 2007-4506, June 2007.

[4] Andino, M. Y., Wallace, R. D., Schmit, R. F., Camphouse, R. C., Myatt, J. H., and Glauser, M. N., "Flow and Aero-Optics Around a Turret Part 1: Open Loop Flow Control," 39th Plasmadynamics and Lasers Conference, Seattle, WA, AIAA Paper 2008-4216, June 2008.

[5] Glauser, M., Higuchi, H., Ausseur, J., Pinier, J., and Carlson, H., "Feedback Control of Separated Flows," 2nd AIAA Flow Control Conference, Portland, OR, AIAA Paper 2004-2521, June 2004.

[6] Pinier, J. T., Ausseur, J. M., Glauser, M. N., and Higuchi, H.,

"Proportional Closed-Loop Feedback Control of Flow Separation," *AIAA Journal*, Vol. 45, No. 1, 2007, pp. 181–190. doi:10.2514/1.23465

[7] Wallace, R. D., Andino, M. Y., Glauser, M., Camphouse, R. C., Schmit, R. F., and Myatt, J. H., "Flow and Aero-Optics Around a Turret Part 2: Surface Pressure Based Proportional Closed Loop Flow Control," 39th Plasmadynamics and Lasers Conference, Seattle, WA, AIAA Paper 2008-4217, June 2008.

[8] Morgan, P. E., and Visbal, M. R., "Numerical Simulations Investigating Control of Flow Over a Turret," 47th AIAA Aerospace Sciences Meeting, Orlando, FL, AIAA Paper 2009-574, Jan. 2009.

[9] Smits, A. J., and Dussauge, J.-P., *Turbulent Shear Layers in Supersonic Flow*, 2nd ed., Springer, New York, 2006.

[10] Thirunavukkarasu, V., Carlson, H., Wallace, R., Shea, P., and Glauser, M., "Measurement and Dynamical Model-Based Feedback Flow Control Development and Simulation for a Pitching Turret," *AIAA Journal* (accepted for publication).

[11] Adrian, R. J., "On the Role of Conditional Averages in Turbulence Theory," *Turbulence in Liquids; Proceedings of the Fourth Biennial Symposium on Turbulence in Liquids*, edited by J. Zakin, and G. Patterson, Science Press, Marrickville, New South Wales, Australia, 1977, pp. 323–332.

[12] Carlson, H., and Miller, R., "Reduced-order Modeling and Sensing of Flow Separation on Lifting Surfaces," 40th AIAA Aerospace Sciences Meeting and Exhibit, Reno, NV, AIAA Paper 2002-0975, Jan. 2002.

[13] Taylor, J., and Glauser, M., "Towards Practical Flow Sensing and Control via POD and LSE Based Low-Dimensional Tools," *Journal of Fluids Engineering*, Vol. 126, No. 3, 2004, pp. 337–345. doi:10.1115/1.1760540

A. Naguib
Associate Editor